RESEARCH ARTICLE
Host-Microbe Biology

The Human Sodium Iodide Symporter as a Reporter Gene for Studying Middle East Respiratory Syndrome Coronavirus Pathogenesis

Svetlana Chefer,[a] Jurgen Seidel,[a] Adam S. Cockrell,[b] Boyd Yount,[b] Jeffrey Solomon,[c] Katie R. Hagen,[a] David X. Liu,[a] Louis M. Huzella,[a] Mia R. Kumar,[d] Elena Postnikova,[a] J. Kyle Bohannon,[a] Matthew G. Lackemeyer,[a] Kurt Cooper,[a] Ariel Endlich-Frazier,[d] Heema Sharma,[d] David Thomasson,[a] Christopher Bartos,[a] Philip J. Sayre,[a] Amy Sims,[b] Julie Dyall,[a] Michael R. Holbrook,[a] Peter B. Jahrling,[a,d] Ralph S. Baric,[b] Reed F. Johnson[d]

[a]Integrated Research Facility, National Institute of Allergy and Infectious Diseases, National Institutes of Health, Frederick, Maryland, USA

[b]Department of Epidemiology, University of North Carolina—Chapel Hill, Chapel Hill, North Carolina, USA

[c]Clinical Research Directorate/Clinical Monitoring Research Program, Leidos Biomedical Research, Inc., Frederick National Laboratory for Cancer Research, Frederick, Maryland, USA

[d]Emerging Viral Pathogens Section, Laboratory of Immunoregulation, Division of Intramural Research, National Institute of Allergy and Infectious Diseases, National Institutes of Health, Frederick, Maryland, USA

ABSTRACT Single photon emission computed tomography (SPECT) is frequently used in oncology and cardiology to evaluate disease progression and/or treatment efficacy. Such technology allows for real-time evaluation of disease progression and when applied to studying infectious diseases may provide insight into pathogenesis. Insertion of a SPECT-compatible reporter gene into a virus may provide insight into mechanisms of pathogenesis and viral tropism. The human sodium iodide symporter (hNIS), a SPECT and positron emission tomography reporter gene, was inserted into Middle East respiratory syndrome coronavirus (MERS-CoV), a recently emerged virus that can cause severe respiratory disease and death in afflicted humans to obtain a quantifiable and sensitive marker for viral replication to further MERS-CoV animal model development. The recombinant virus was evaluated for fitness, stability, and reporter gene functionality. The recombinant and parental viruses demonstrated equal fitness in terms of peak titer and replication kinetics, were stable for up to six *in vitro* passages, and were functional. Further *in vivo* evaluation indicated variable stability, but resolution limits hampered *in vivo* functional evaluation. These data support the further development of hNIS for monitoring infection in animal models of viral disease.

IMPORTANCE Advanced medical imaging such as single photon emission computed tomography with computed tomography (SPECT/CT) enhances fields such as oncology and cardiology. Application of SPECT/CT, magnetic resonance imaging, and positron emission tomography to infectious disease may enhance pathogenesis studies and provide alternate biomarkers of disease progression. The experiments described in this article focus on insertion of a SPECT/CT-compatible reporter gene into MERS-CoV to demonstrate that a functional SPECT/CT reporter gene can be inserted into a virus.

KEYWORDS MERS, coronavirus, medical imaging, reporter gene

Recombinant viruses expressing reporter genes such as luciferase or fluorescent proteins or viral proteins fused with a reporter protein have been used as screening tools for countermeasures and to understand pathogenesis (1–4). While the application of reporter gene technology has provided insight into viral pathogenesis, these exper-

Received 28 September 2018 **Accepted** 26 October 2018 **Published** 12 December 2018

Citation Chefer S, Seidel J, Cockrell AS, Yount B, Solomon J, Hagen KR, Liu DX, Huzella LM, Kumar MR, Postnikova E, Bohannon JK, Lackemeyer MG, Cooper K, Endlich-Frazier A, Sharma H, Thomasson D, Bartos C, Sayre PJ, Sims A, Dyall J, Holbrook MR, Jahrling PB, Baric RS, Johnson RF. 2018. The human sodium iodide symporter as a reporter gene for studying Middle East respiratory syndrome coronavirus pathogenesis. mSphere 3:e00540-18. https://doi.org/10.1128/mSphere.00540-18.

Editor Matthew B. Frieman, University of Maryland, College Park

Address correspondence to Reed F. Johnson, johnsonreed@niaid.nih.gov.

iments are frequently hampered by sacrificing the subject to identify the source of the reporter gene signal (5–7). Applying medical imaging technology, such as single photon emission computed tomography (SPECT) or positron emission tomography (PET), to animal models of human infectious disease provides the capability to serially monitor anatomical and physiological responses to infection in the same subject that can be clinically translated. Generating a virus that carries a SPECT/PET-compatible reporter gene furthers that capability by serial, real-time evaluation of virus kinetics, identification of tissue tropism, and determination of pathogenic mechanisms. The human sodium iodide symporter (*hNIS*) gene has emerged as one of the most promising reporter genes in preclinical and translational research for oncology and gene therapy (8, 9).

The hNIS symporter is an intrinsic plasma membrane protein belonging to the sodium/solute symporter family, which drives negatively charged solutes into the cytoplasm using a sodium ion electrochemical gradient (10). The advantages of *hNIS* as an imaging reporter gene include its relatively small size (~2 kb), wide availability of substrates, such as radioiodines, tetrafluoroborate, and ^{99m}Tc-pertechnetate, and well-understood metabolism and clearance mechanisms of these substrates (11). Oncolytic viruses such as measles virus and replication-deficient adenovirus that contain *hNIS* have demonstrated value as theranostics, as *hNIS* is used both as a therapeutic platform and to track the therapeutic effect (8, 9). In addition, hNIS is unlikely to perturb the underlying cell biochemistry, and no negative effects of resultant sodium influx have been observed (12). Finally, once incorporated into the viral genome, the relatively small size of the reporter gene is less likely than larger reporter genes to alter viral pathogenic properties (13).

Middle East respiratory syndrome-CoV (MERS-CoV) recently emerged and is associated with Middle East respiratory syndrome (MERS), a severe, frequently lethal pneumonia in humans (14–16). Viral pathogenesis is not well understood, in part, because of limited autopsy information and a lack of animal models that fully recapitulate human disease. As with most lethal infectious diseases, animal models are the cornerstone for preclinical countermeasure evaluation and understanding pathogenesis. MERS-CoV provides a unique opportunity to incorporate reporter gene technology to better understand viral pathogenesis because its larger genome size may be more amenable to reporter gene insertion than other viruses.

Animal models for MERS are under development with no single model identified as the standard. New World and Old World nonhuman primates infected with MERS-CoV develop transient respiratory disease with little or no virus replication and varying disease outcome (17–19). MERS-CoV-exposed New Zealand White rabbits develop limited lung pathology with evidence of viral replication but did not show overt clinical signs of disease (20, 21). Transgenic mice globally expressing the human CD26/dipeptidyl peptidase 4 (DPP4) receptor (22), expressing the human receptor under the murine promoter (23) or transduced with DPP4 receptor (24) become permissive to the virus but do not develop fulminant, lethal respiratory disease. Therefore, changes in reporter gene signal may serve as a biomarker for countermeasure evaluation.

The objective of this study was to incorporate *hNIS* into MERS-CoV to improve the MERS animal models. Incorporation of a SPECT/PET-compatible reporter gene with an emerging virus such as MERS-CoV requires functional evaluation of the recombinant virus to ensure similar fitness to the parental pathogen. We hypothesized that insertion of hNIS would result in stable expression of a SPECT/PET-compatible reporter gene. A recombinant MERS-CoV carrying *hNIS* (rMERS-CoV/*hNIS*) was generated. We assessed the stability, fitness, and functionality of this recombinant pathogen *in vitro* and in CRISPR-generated transgenic mice that support replication of wild-type MERS-CoV (25).

RESULTS

rMERS-CoV/*hNIS* genetic stability, kinetics, and fitness. Recombinant virus was evaluated by one-step and multistep kinetics and by serial passaging of the virus. rMERS-CoV/*hNIS* replicated similarly to rMERS-CoV in Vero E6 cells infected at a multi-

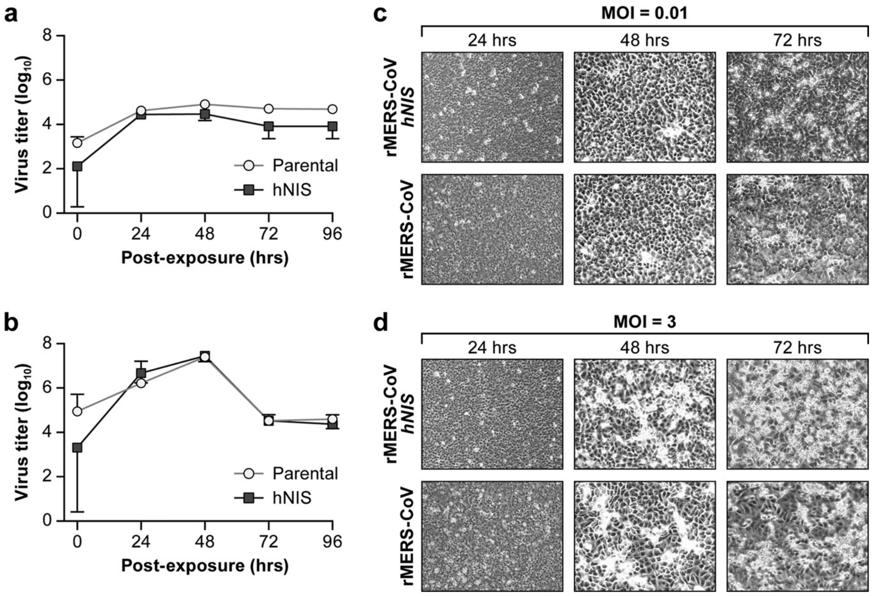

FIG 1 Kinetics of rMERS-CoV/*hNIS* and parental rMERS-CoV replication in Vero E6 cells. (a and b) Multistep (a) and one-step (b) growth curves of Vero E6 cells infected with rMERS-CoV (Parental) and rMERS-CoV/*hNIS* (*hNIS*). Quantification of the release of infectious virus at the indicated time points (hours postexposure) was determined by plaque assays. Each data point represents the mean ± standard deviation (SD) (error bar) averaged from three independent experiments. (c and d) Cytopathology of rMERS-CoV and rMERS-CoV/*hNIS* in Vero E6 cells. The cells were infected with either rMERS-CoV or rMERS-CoV/*hNIS* at an MOI of 0.01 (c) or 3 (d) and analyzed by light microscopy at the indicated time points. Photomicrographs were taken using a 40× objective.

plicity of infection (MOI) of 0.01 with a peak in virus yield of 4 $\log_{10}$ plaque-forming units (PFU)/ml at 24 h. At an MOI of 3, viral yields peaked at 7 $\log_{10}$ PFU/ml at 48 h and plateaued at 72 h postinfection (Fig. 1a and b). The correlations between the multistep growth curves for cells infected at an MOI of 0.01 g ($r = 0.96$ Pearson correlation, $P = 0.0082$) (Fig. 1a) and one-step growth curves of cells infected at an MOI of 3 ($r = 0.90$, $P = 0.03$) (Fig. 1b) for both viruses were high. Both viruses had comparable cytopathic effects (Fig. 1c and d).

Expression of the *hNIS* transgene was evaluated by reverse transcriptase PCR (RT-PCR) using primers to specifically detect hNIS expression by MERS-CoV. The resulting 635-bp PCR product includes the MERS-CoV leader sequence and a portion of the *hNIS* transgene. RT-PCR confirmed *hNIS* expression in rMERS-CoV/*hNIS*-infected Vero E6 cells up to 96 h (Fig. 2a). The PCR product was not detected in parental rMERS-CoV-infected cells (Fig. 2b). The RT-PCR assay was also performed to determine the stability of the *hNIS* transgene following serial passage. The hNIS transgene was stable in rMERS-CoV/hNIS for up to six cell culture passages (Fig. 2c).

hNIS functionality in MERS-CoV/*hNIS*-infected cells. To demonstrate *in vitro* hNIS functionality, a series of assays were performed to characterize the kinetics of ^{99m}Tc-pertechnetate cellular uptake, the relationship between virus concentration and probe cellular uptake, and between probe dose and its detectability by the gamma camera. The *in vitro* hNIS functionality assay is outlined in Fig. 3a and b. The ^{99m}Tc-pertechnetate uptake by rMERS-CoV/*hNIS*-infected cells in six-well plates was visible on the tissue culture plate images and distinguishable from the background radioactivity in the wells with uninfected and rMERS-CoV-infected cells (Fig. 3c). In rMERS-CoV/*hNIS*-infected cells, uptake increased with time after infection and reached a maximum, 20% of the dose applied to the well, at the final 96-h postinfection time point (Fig. 4a). The mean radioactivity values measured in the wells were 89.8 ± 5.6, 0.77 ± 0.15, and 0.57 ± 0.04 μCi for rMERS-CoV/*hNIS*-infected, rMERS-CoV-infected, and uninfected cells, respectively.

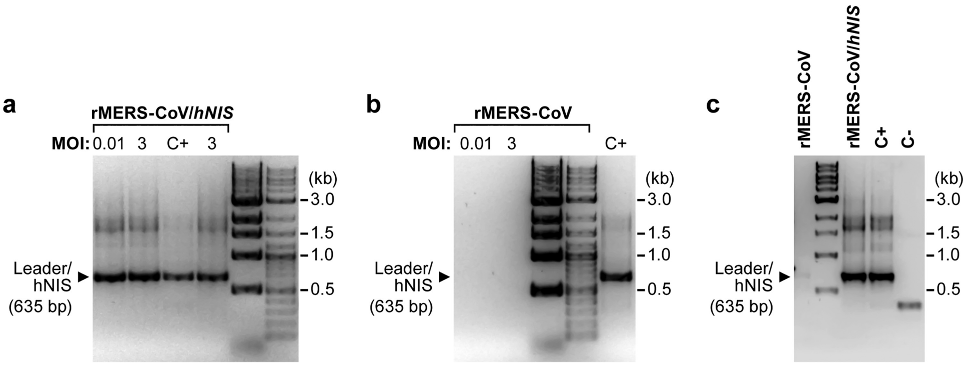

FIG 2 Retention of *hNIS* transgene following viral kinetics analysis and serial passage. (a and b) Vero E6 cells were infected with rMERS-CoV/hNIS (a) or parental rMERS-CoV (b) at an MOI of 0.01 or 3 and then collected at 96 h postinfection for RT-PCR. (c) Retention of the *hNIS* gene following serial passage. RNA was extracted from cells 72 h postinfection followed by RT-PCR at passage 6. A positive-control virus (C+) and uninfected negative-control cells (C−) were used as controls.

^{99m}Tc-pertechnetate uptake was dependent on the virus MOI (Fig. 4b). Higher MOI was associated with greater accumulation of ^{99m}Tc-pertechnetate by rMERS-CoV/*hNIS*-infected cells.

Uptake by rMERS-CoV/*hNIS*-infected cells was also dependent on the dose of ^{99m}Tc-pertechnetate (Fig. 4c). The relationship between radioactivity measured by the gamma camera on plate images and the dose of ^{99m}Tc-pertechnetate added to each well was linear with high correlation ($R^2 = 0.99$, linear regression). At 96 hours postinfection with an MOI of 0.01, uptake was slightly above the background level when the ^{99m}Tc-pertechnetate dose of 0.02 mCi per well was applied, and no uptake was detected when 0.004 mCi of ^{99m}Tc-pertechnetate was added to each well (Fig. 4c). Therefore, the ^{99m}Tc-pertechnetate dose should be considered a limiting factor for detection of *hNIS* expression in rMERS-CoV/*hNIS*-infected cells. Importantly, no changes

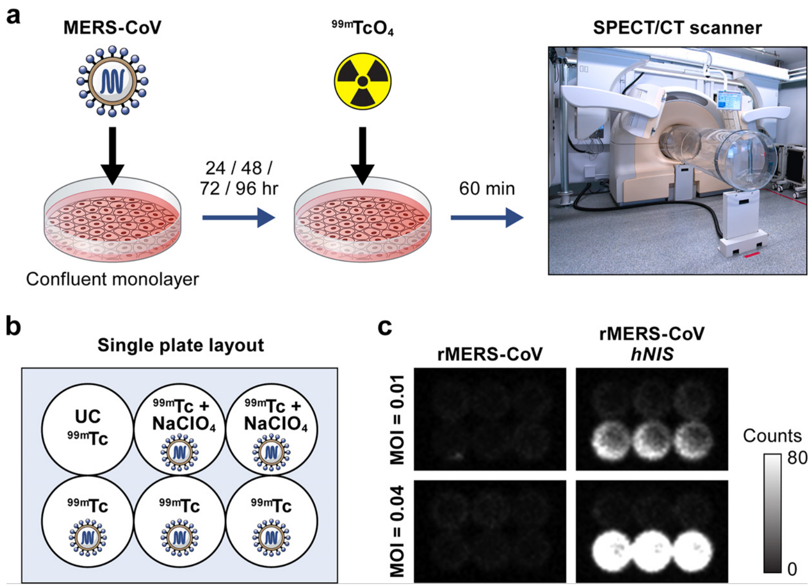

FIG 3 Radio-uptake of ^{99m}Tc-pertechnetate by planar scintigraphy. (a) Experimental overview of *in vitro* evaluation of the rMERS-CoV/*hNIS* virus. Vero E6 cells were infected with rMERS-CoV or rMERS-CoV/*hNIS* at an MOI of 0.01 or 0.04. At various time points postinfection, the cells were incubated with ^{99m}Tc-pertechnetate, and images of the plates were acquired. (b) Plate layout for hNIS functional assays. (c) Representative images of the plates acquired at 24 h postinfection at an MOI of 0.01 (top plates) or 0.04 (bottom plates) after incubation with ^{99m}Tc-pertechnetate.

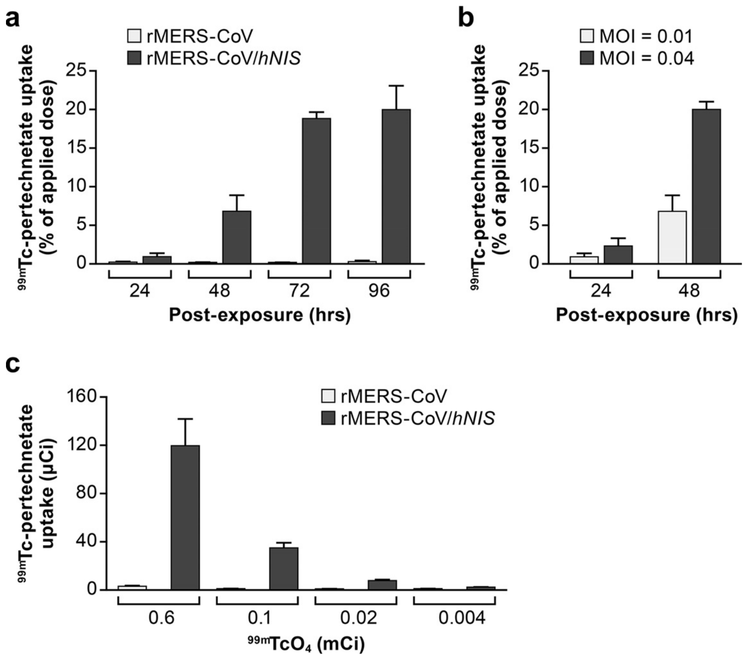

FIG 4 Quantification of ^{99m}Tc-pertechnetate uptake by rMERS-CoV/*hNIS*-infected cells. (a) ^{99m}Tc-pertechnetate uptake by rMERS-CoV- or rMERS-CoV/*hNIS*-infected cells at an MOI of 0.01 at 24, 48, 72, and 96 h postinfection. (b) ^{99m}Tc-pertechnetate uptake by rMERS-CoV/*hNIS*-infected cells at an MOI of 0.01 or 0.04 at 24 and 48 h postinfection. (c) Quantitative analysis of ^{99m}Tc-pertechnetate uptake applied at doses ranging from 0.6 to 0.004 mCi per well.

in ^{99m}Tc-pertechnetate accumulation were detected in the wells infected with the parental virus rMERS-CoV regardless of the dose.

The specificity of ^{99m}Tc-pertechnetate uptake by rMERS-CoV/*hNIS*-infected cells was confirmed by adding sodium perchlorate, a specific and competitive inhibitor of hNIS protein function, and assessing uptake at 24 h postinfection (Fig. 5a). At a concentration of 0.1 mM, sodium perchlorate blocked 99.5% of the cellular uptake of ^{99m}Tc-pertechnetate in rMERS-CoV/*hNIS*-infected cells at an MOI of 0.01. Sodium perchlorate concentrations below 0.1 mM reduced the inhibitory effect. For example, radiotracer uptake was inhibited by 50% at sodium perchlorate concentrations of 0.001 mM at 24 h postinfection (Fig. 5a). The effective inhibition of ^{99m}Tc-pertechnetate uptake with 0.1 mM sodium perchlorate declined between 48 and 96 h postinfection (Fig. 5b), suggesting that viral transcription can overcome the inhibitory effect. By 96 h postinfec-

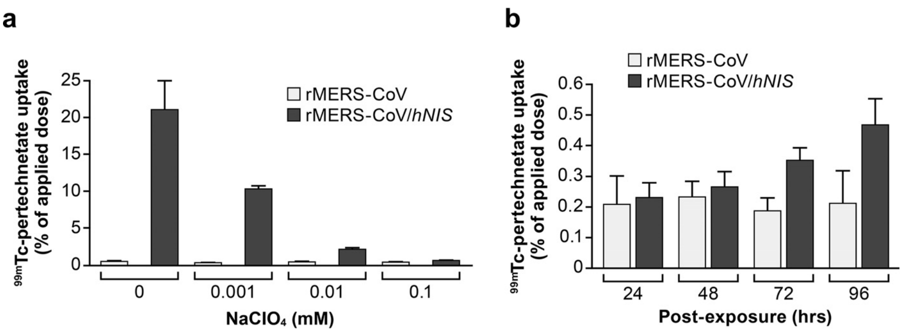

FIG 5 Sodium perchlorate-mediated inhibition of ^{99m}Tc-pertechnetate uptake. (a) Quantitation of ^{99m}Tc-pertechnetate uptake in the presence of sodium perchlorate at doses ranging from 0 and 0.1 mM. ^{99m}Tc-pertechnetate uptake was reduced in rMERS-CoV/*hNIS*-infected cells with increasing sodium perchlorate concentrations. (b) ^{99m}Tc-pertechnetate uptake by rMERS-CoV- or rMERS-CoV/*hNIS*-infected cells at an MOI of 0.01 at 24, 48, 72, and 96 h postinfection in the presence of 0.1 mM sodium perchlorate.

tion, ^{99m}Tc-pertechnetate uptake in rMERS-CoV/*hNIS*-infected cells was nearly double the uptake at 24 h postinfection in the presence of sodium perchlorate (Fig. 5b).

***In vivo* evaluation of rMERS-CoV/*hNIS*.** CRISPR-generated 288/330$^{+/+}$ DPP4 humanized mice were challenged with parental rMERS-CoV or rMERS-CoV/*hNIS* by the intranasal route and monitored by SPECT imaging. One group each of mice infected with rMERS-CoV/*hNIS* and parental rMERS-CoV were euthanized on day 3 postexposure (pe), while another set was monitored to day 7 pe and euthanized. SPECT/CT imaging was performed to determine whether sites of virus replication were evident in these animals. Unfortunately, the low resolution of the clinical scanner used in our biocontainment facility prevented clear discrimination of *hNIS*-expressing tissues and limited the utility of the imaging. Details of the SPECT/CT data can be found in Fig. S1 and the methodology is described in Text S1 in the supplemental material.

Macroscopic evaluation of the lungs from virus- and sham-exposed animals did not reveal any significant pathological changes except in one of the five mice in group 2 (rMERS-CoV). The right caudodorsal lung lobe of this animal was congested. Microscopically, minimal-to-mild perivascular and peribronchiolar inflammation was noted multifocally with variable congestion in rMERS-CoV- and rMERS-CoV/*hNIS*-infected mice (Fig. 6a to e). Kidney congestion was also noticeable in 40 and 50% of mice in groups 2 and 3, respectively, on day 3 pe and 33 and 50% on day 7 pe in mice in groups 4 and 5, respectively, infected with rMERS-CoV or rMERS-CoV/*hNIS* (Table 1). The percentage of mice with alterations in the lung was higher on day 7 pe compared to that observed on day 3 pe (100% vs $<$83%, respectively). Extensive focal congestion in the lungs and multifocal congestion in the kidneys were observed in one of five mice from group 1 receiving sham infection, but inflammation was not manifested in this group (Table 1).

Infectious virus could be detected only in the lungs from 3/6 mice from group 3 (5.01 ± 0.45 $\log_{10}$ PFU/mg) but was detected in the lung tissue by plaque assay in 4 of 5 mice from group 2 (6.7 ± 0.43 $\log_{10}$ [mean ± SD] PFU/mg) (Fig. 6f). The differences in viral loads between groups 2 and 3 were not statistically significant (two-tailed *t* test, $P = 0.214$). RT-PCR indicated maintenance of the *hNIS* transgene in 3 of 6 mice in group 3 (Fig. 6g). The inability to detect virus in 3 of 6 mice and the nearly 2 $\log_{10}$ decrease in PFU/mg observed for rMERS-CoV/*hNIS* at day 3 supports a loss of viral fitness *in vivo*. Virus could not be detected by plaque assay or RT-PCR at 7 days postinfection.

DISCUSSION

This is the first report describing the application of a recombinant RNA virus expressing a SPECT/PET reporter gene to study viral pathogenesis. Our data demonstrate the feasibility of using hNIS as a reporter protein in animal models of human disease, provided a higher-resolution SPECT/CT or PET/CT is available. Despite the presence of a robust signal, the clinical grade SPECT/CT in our facility did not provide the necessary resolution to demonstrate *in vivo* functionality of the rMERS-CoV/*hNIS* in mice. If available, a micro-PET/CT and the use of tetrafluorborate, an alternate hNIS ligand, could be used to increase sensitivity and improve signal to noise (26). The recombinant MERS-CoV/*hNIS* has similar fitness to the parental virus, rMERS-CoV, as evidenced by similar kinetics, fitness, and cytopathic effect *in vitro*. The results of *in vivo* evaluation also support similar fitness; however, further development would require insertion of the hNIS transgene into other locations within the virus and insertion of the transgene into the MERS-15 virus, which can cause lethal respiratory disease in the 288/300^{++} mice.

Genetic stability of the *hNIS* transgene cloned into MERS-CoV was confirmed over six *in vitro* passages. hNIS maintained its function in rMERS-CoV/*hNIS*-infected cells upon incubation with ^{99m}Tc-pertechnetate. The probe uptake (percentage of radioactive dose applied to each well) positively correlated with virus concentration and time postinfection. rMERS-CoV/*hNIS* expression of the hNIS protein in infected Vero E6 cells resulted in specific uptake of ^{99m}Tc-pertechnetate and kinetics that correlated with viral replication. Similarly, in a previous study using *hNIS*-expressing adenoviral vector in

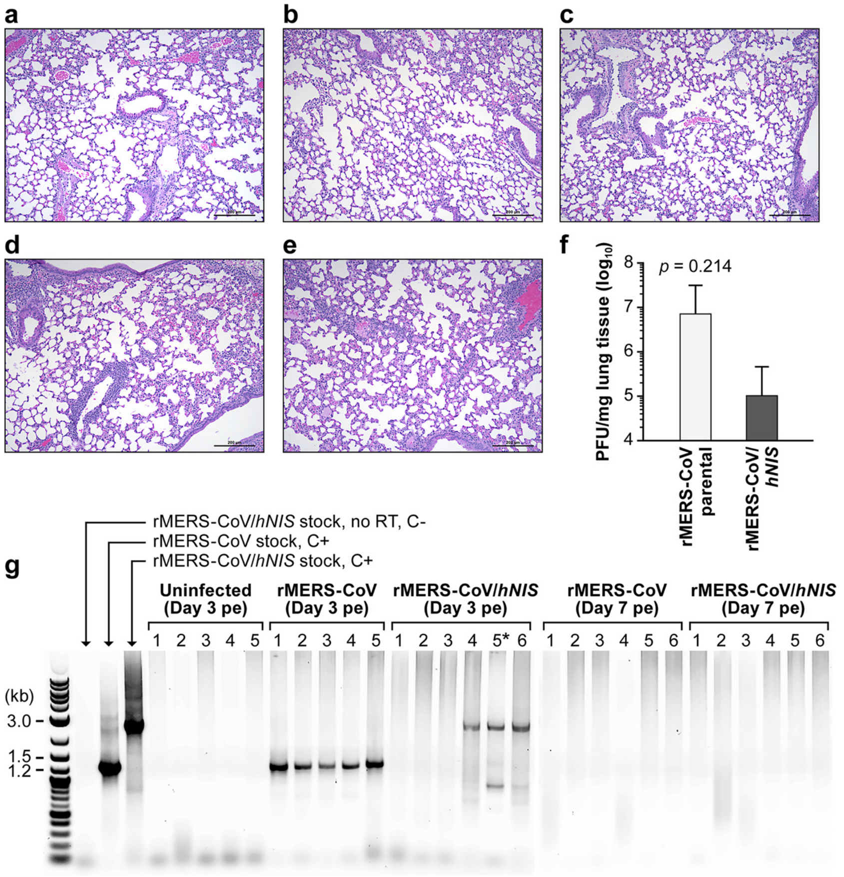

FIG 6 Lung histopathology in infected mice and detection of rMERS-CoV/*hNIS* or rMERS-CoV in lung tissue. (a to e) Histopathology of the lungs of one representative mouse each from groups 1, 2, 3, 4, and 5 infected with rMERS-CoV or MERS-CoV/*hNIS*. The cells were visualized with HE stain. Magnification, ×10. Bars = 200 μm. (a) Uninfected control mouse. (b) Representative mouse infected with rMERS-CoV (group 1) with multifocal, minimal-to-mild perivascular and peribronchiolar inflammation, with congestion on day 3 postexposure (pe). (c) Representative mouse infected with rMERS-CoV/hNIS (group 2) with multifocal, minimal-to-mild perivascular and peribronchiolar inflammation, with congestion on day 3 pe. (d) Representative mouse infected with rMERS-CoV (group 4) with multifocal, minimal-to-mild perivascular and peribronchiolar inflammation with congestion at day 7 pe. (e) Representative mouse infected with rMERS-CoV/hNIS (group 5) with multifocal, minimal-to-mild perivascular and peribronchiolar inflammation with congestion at day 7 pe. (f) Viral load in lung tissue on day 3 pe in mice infected with rMERS-CoV or rMERS-CoV/*hNIS* as determined by plaque assay. (g) RT-PCR analysis of the lungs recovered from rMERS-CoV/*hNIS*- or rMERS-CoV-infected mice. The leftmost lane contains molecular size markers (in kilobases). The next three lanes contain stock controls, rMERS-CoV/*hNIS* (stock control, without RT step), rMERS-CoV stock, and rMERS-CoV/*hNIS* stock. C+ indicates positive-control virus, and C− indictes uninfected negative-control cells. Samples from groups 1 to 5 are shown in the five sets of lanes as follows: group 1, uninfected control (C−) group, lanes 1 to 5; group 2, exposed to rMERS-CoV, lanes 1 to 5; group 3, exposed to rMERS-CoV/*hNIS*, lanes 1 to 6; group 4, exposed to rMERS-CoV, lanes 1 to 5; group 5, exposed to rMERS-CoV/*hNIS*, lanes 1 to 6. The asterisk in lane 5* of the rMERS-CoV/*hNIS*-treated group on day 3 pe indicates altered PCR conditions (48°C annealing temperature, 3% dimethyl sulfoxide) to improve the sensitivity to detect rMERS-CoV/*hNIS*.

carcinoma cells, radionuclide accumulation of ^{99m}Tc-pertechnetate correlated with the amount of adenovirus delivered and the activity of the added radioisotope (27).

Consistent with other studies (28), sodium perchlorate greatly decreased rMERS-CoV/*hNIS* uptake in cell culture. However, the sodium perchlorate dose that blocked hNIS protein function by 99.5% at 24 h postinfection became less effective at +96 h postinfection, corresponding with increased viral replication, and presumably symporter expression from the virus.

These experiments utilized the 288/330$^{+/+}$ transgenic humanized mice (25). Results from previous work indicated that these mice, when challenged with the mouse-adapted MERS-15 virus, developed severe acute respiratory distress syndrome, includ-

TABLE 1 Pathological summary of mice

Mouse group (*n*)	Recombinant virus	Day of tissue sampling	% mice in group with lung inflammation (*n*)		% mice in group with congestion (*n*)	
			Minimal	Mild	Lung	Kidney
Group 1 (5)	None (sham)	7	0	0	20 (1)	20 (1)
Group 2 (5)	rMERS-CoV	3	40 (2)	40 (2)	80 (4)	40 (2)
Group 3 (6)	rMERS-CoV/hNIS	3	33 (2)	33 (2)	83 (4)	50 (3)
Group 4 (6)	rMERS-CoV	7	33 (2)	50 (3)	100 (6)	33 (2)
Group 5 (6)	rMERS-CoV/hNIS	7	17 (1)	67 (4)	100 (6)	50 (3)

ing decreased survival, extreme weight loss, decreased pulmonary function, pulmonary hemorrhage, and pathological signs indicative of end-stage lung disease (25). Similar to the previously published work, the parental (MERS-CoV) and recombinant virus (MERS-CoV/*hNIS*) grew to high titers in the 288/330$^{+/+}$ mice, but the mice did not develop disease (25). Although the SPECT signal was dependent on the viral load in tissue culture, the SPECT signal from infected mice as determined by comparing lung-to-heart ratios was not sufficiently different between infected and uninfected mice. Unfortunately, rMERS-CoV/*hNIS* was detected by PCR in only 50% of infected mice on day 3 pe, suggesting limited *in vivo* genetic stability.

This inconsistent detection of rMERS-CoV/*hNIS* could be due to *hNIS* transgene insertion into the ORF5 gene, which antagonizes innate immunity and thus may impact viral pathogenesis *in vivo* (29). Cockrell et al. demonstrated that a clone of the MERS-15 virus with an ORF5 deletion was attenuated compared to a clone in which the ORF5 gene was not deleted (25). This attenuation may also explain the lower titer in the rMERS-CoV/*hNIS* mice compared to that observed with the parental virus (Fig. 6f). Further utilization of *hNIS* as a reporter for virus growth and localization would include developing the mouse-adapted version (rMERS-15/*hNIS*-CoV) for evaluation and model improvement and insertion of the *hNIS* into other locations of the viral genome.

Imaging with a small-animal PET scanner and PET radiotracer ^{18}F-tetrafluoroborate would improve image quality and sensitivity for visualizing rMERS-CoV/*hNIS* replication. An alternative to the SPECT is use of a gamma counter to measure the radioactivity in the tissues; unfortunately, a suitable gamma counter is not available in our biosafety level 4 (BSL-4) laboratory. Alternatively, utilization of rMERS-CoV/*hNIS* in larger animals, i.e., nonhuman primates, should help overcome the SPECT clinical scanner's limited spatial resolution. This technology also aids identification of tissues that are directly infected, which would improve virological analysis, histological analysis, and characterization of tissue-specific response to infection.

Although the animal models of MERS require further improvement, the model chosen for this experiment was useful in supporting the relative *in vivo* stability of the *hNIS* reporter in MERS-CoV. The results from the mouse experiments agree with published studies (20, 21, 25) and corroborate previous data that indicate that wild-type virus grows to a high titer in the 288/300^{++} transgenic mice. Realizing the potential and limitations of the existing MERS-CoV animal models, further incorporation of real-time imaging technology will expand MERS-CoV research. Development of recombinant viruses with imaging reporter genes and its application with suitable animal models will be instrumental in furthering our understanding of viral pathogenesis, potentially leading to improved animal models of human disease and more efficient countermeasure evaluation.

MATERIALS AND METHODS

Cells, viruses, and animals. Recombinant parental virus (rMERS-CoV) and MERS-CoV expressing *hNIS* (rMERS-CoV/*hNIS*) were generated as previously described (30). Briefly, the *hNIS* open reading frame (ORF) was inserted into the NS5 ORF of MERS-CoV. The nine bases, UCCUUCAUA, between the M gene TRS and its start codon were included at the start of the *hNIS* sequence and cloned using the SanDI restriction enzyme site upstream of ORF 6. Transfections for recovery of the recombinant viruses were performed at biosafety level 3 (BSL-3). Except for generation of the recombinant viruses, all experimental procedures were conducted at BSL-4 biocontainment laboratories due to the location of the SPECT clinical scanner. MERS-CoV isolate Hu/Jordan-N3/2012 was propagated in MRC-5 cells (ATCC) at a multiplicity of infection (MOI) of 0.1 for 5 days following published procedures (19, 31). Virus was recovered by removal of the tissue culture media followed by centrifugation, titers of the virus were determined by plaque assay, and the cultures were evaluated for mycoplasma and endotoxin contamination (19, 31). Vero E6 cells (ATCC CRL-1586) were maintained in Dulbecco's modified Eagle medium (DMEM) (Lonza) supplemented with 5% fetal bovine serum (FBS) and incubated at 37°C and 5% CO_2 without antibiotics or antimycotics.

CRISPR-Cas9-engineered mice (288/330$^{+/+}$; $n = 30$) encoding two amino acids (positions 288 and 330) that match the human sequence in the DPP4 receptor on both chromosomes were obtained from the University of North Carolina (25).

rMERS-CoV and rMERS-CoV/*hNIS* plaque assays. Plaque assays were performed in Vero E6 cells as previously described (32). For titration of virus in tissues, the collected tissues were homogenized using a bead-based tissue homogenizer to make a 10% homogenate in DMEM plus 2% FBS (Sigma).

One-step and multistep growth curves and serial passage. Kinetic studies with rMERS-CoV and rMERS-CoV/*hNIS* were performed in parallel experiments in triplicate. Vero E6 cells were infected with rMERS-CoV or rMERS-CoV/*hNIS* at an MOI of 0.01 or 3. Samples were collected at 0, 24, 36, 48, 72, and 96 h postinfection, and virus titers were determined as described above. Serial passage was performed to demonstrate stability of the *hNIS* transgene. Virus was passaged every 72 h for six passages. An aliquot was collected and assayed by reverse transcriptase PCR (RT-PCR) to detect the *hNIS* transgene.

RT-PCR of viral RNA. For evaluation of stability of the *hNIS* gene, total RNA was isolated from Vero E6 cells collected 24, 36, 48, 72, and 96 h after rMERS-CoV and rMERS-CoV/*hNIS* infection at MOIs of 0.01 and 3. The RNA was reverse transcribed into cDNA using deoxythymidine oligonucleotide primers and SuperScript reverse transcriptase II (Thermo Fisher Scientific) according to the manufacturer's protocol. Two custom primers, *hNIS* Leader (forward primer sequence, 5′CTATCTCACTTCCCCTCGTTCTC) with *hNIS*6 (reverse primer sequence, 5′GAAGCCACTTAGCATCAC) were used to create PCR products. PCR products were separated and identified on a SYBR safe DNA-stained agarose gel (Thermo Fisher Scientific). Stock rMERS-CoV/*hNIS* was used as a positive control, and uninfected-cell lysates were used as a negative control for RT-PCR.

Cell culture radio-uptake assay. Functionality of the *hNIS* gene was assessed by *hNIS*-mediated accumulation of ^{99m}Tc-pertechnetate by rMERS-CoV/*hNIS*-infected cells. Vero E6 cells were infected with rMERS-CoV or rMERS-CoV/*hNIS* at two different MOIs, 0.01 and 0.004, and incubated for 0, 24, 36, 48, 72, and 96 h. ^{99m}Tc-pertechnetate, 0.004 to 0.6 mCi in 0.2 ml, was added to each well and incubated for 60 min. ^{99m}Tc-pertechnetate was removed from the wells, and the cells were washed with room temperature media. Planar images of the plates were acquired over 30 min with a single gamma camera head using the Precedence SPECT/computed tomography (CT) clinical system (Philips Medical Systems), that was modified to operate in a biocontainment environment (33). The *in vitro* samples were quantified using the SPECT/CT scanner. Uninfected cells were treated with ^{99m}Tc-pertechnetate to determine the background level. Specificity of ^{99m}Tc-pertechnetate uptake by rMERS-CoV/*hNIS*-infected cells was assessed by adding sodium perchlorate, $NaClO_4$, 1 to 100 μM, to the wells prior to ^{99m}Tc-pertechnetate introduction. ^{99m}Tc-pertechnetate counts from each well were converted into radioactivity units and decay-corrected relative to the time of probe introduction to the wells. Uptake of ^{99m}Tc-pertechnetate by infected cells was expressed as a percentage of the radioactive dose applied to the well. The radio-uptake assays were conducted in triplicate.

Transgenic mouse experiments. Thirty 288/330$^{+/+}$ mice, 15 males and 15 females, were split into 5 groups of 6 animals. Two mice, one from group 1 and one from group 4, did not recover from anesthesia after a preexposure scan and were not replaced. Mice were lightly anesthetized with isoflurane and were exposed intranasally with phosphate-buffered saline (PBS) without virus (group 1) or with rMERS-CoV (groups 2 and 4) or rMERS-CoV/*hNIS* (groups 3 and 5). The virus/PBS was instilled into both nostrils, 25 μl per nostril. The mice were monitored daily for clinical signs of disease. The animals from groups 2 and 3 were euthanized on day 3 postexposure (pe), and the animals from groups 1, 4, and 5 were euthanized on day 7 pe. The lungs were collected for gross pathological and microscopic evaluation and virus detection via plaque assay.

Ethics statement. All work with animals was performed in an AAALAC-accredited research facility and approved by the National Institute for Allergy and Infectious Disease Division of Clinical Research Animal Care and Use Committee. The experiments complied with the Animal Welfare Act regulations, Public Health Service policy, and the *Guide for the Care and Use of Laboratory Animals* (34). Animals were monitored daily. Clinical health, body weight, and food consumption were recorded.

Statistical analysis. Statistical analysis was performed using Graphpad Prism 7.03 (Graphpad Software Inc.) as indicated in the text.

SUPPLEMENTAL MATERIAL

Supplemental material for this article may be found at https://doi.org/10.1128/mSphere.00540-18.

TEXT S1, DOCX file, 0.01 MB.

FIG S1, TIF file, 2.1 MB.

ACKNOWLEDGMENTS

We thank Russell Byrum, Danny Ragland, and Marisa St. Claire and the entire IRF Comparative Medicine and Imaging staff for successful implementation of SPECT scanning procedures in mice in the biosafety level 4 environment. We thank Laura Bollinger for critically editing the manuscript and Jiro Wada for figure development. We also thank Matthias Schnell, Thomas Jefferson University, for his critical review of the manuscript.

This work was funded in part through the NIAID Division of Intramural Research and the NIAID Division of Clinical Research, Battelle Memorial Institute's prime contract with the U.S. National Institute of Allergy and Infectious Diseases (NIAID) under contract HHSN272200700016I and an NIH grant in aid to R.S.B. (AI110700 and AI132178). K.R.H., J.K.B., and M.R.H. performed this work as employees of Battelle Memorial Institute. Subcontractors to Battelle Memorial Institute who performed this work are as follows: S.C., D.T., E.P., and J.D., all employees of Tunnell Government Services, Inc.; M.G.L., an employee of Lovelace Respiratory Research Institute; C.B. and P.J.S., employees of MedRelief; D.L., an employee of Charles River Laboratories.

S.C., C.B., P.J.S., J.D., D.X.L., L.M.H., E.P., J.K.B., A.E.-F., M.G.L., K.C., M.R.K., and J.S. performed experiments and analyzed data. A.S., R.S.B., B.Y., and A.S.C. provided 288-330$^{+/+}$ mice and reagents and generated the recombinant viruses. S.C., K.R.H., M.R.K., M.R.H., D.T., P.B.J., and R.F.J. designed experiments. S.C. and R.F.J. wrote the manuscript. All authors read and edited the manuscript.

We declare that we have no competing financial interests.

The content of this publication does not necessarily reflect the views or policies of the U.S. Department of Health and Human Services (DHHS) or of the institutions and companies affiliated with the authors.

REFERENCES

1. Hoenen T, Groseth A, Callison J, Takada A, Feldmann H. 2013. A novel Ebola virus expressing luciferase allows for rapid and quantitative testing of antivirals. Antiviral Res 99:207–213. https://doi.org/10.1016/j.antiviral.2013.05.017.
2. Marsh GA, Virtue ER, Smith I, Todd S, Arkinstall R, Frazer L, Monaghan P, Smith GA, Broder CC, Middleton D, Wang LF. 2013. Recombinant Hendra viruses expressing a reporter gene retain pathogenicity in ferrets. Virol J 10:95. https://doi.org/10.1186/1743-422X-10-95.
3. Rennick LJ, de Vries RD, Carsillo TJ, Lemon K, van Amerongen G, Ludlow M, Nguyen DT, Yuksel S, Verburgh RJ, Haddock P, McQuaid S, Duprex WP, de Swart RL. 2015. Live-attenuated measles virus vaccine targets dendritic cells and macrophages in muscle of nonhuman primates. J Virol 89:2192–2200. https://doi.org/10.1128/JVI.02924-14.
4. Rozelle DK, Filone CM, Dower K, Connor JH. 2014. Vaccinia reporter viruses for quantifying viral function at all stages of gene expression. J Vis Exp 15:e51522.
5. Altenburg AF, van de Sandt CE, Li BWS, MacLoughlin RJ, Fouchier RAM, van Amerongen G, Volz A, Hendriks RW, de Swart RL, Sutter G, Rimmelzwaan GF, de Vries RD. 2017. Modified vaccinia virus Ankara preferentially targets antigen presenting cells in vitro, ex vivo and in vivo. Sci Rep 7:8580. https://doi.org/10.1038/s41598-017-08719-y.
6. Goff A, Twenhafel N, Garrison A, Mucker E, Lawler J, Paragas J. 2007. In vivo imaging of cidofovir treatment of cowpox virus infection. Virus Res 128:88–98. https://doi.org/10.1016/j.virusres.2007.04.014.
7. Kato SI, Nagata K, Takeuchi K. 2012. Cell tropism and pathogenesis of measles virus in monkeys. Front Microbiol 3:14. https://doi.org/10.3389/fmicb.2012.00014.
8. Ahn BC. 2012. Sodium iodide symporter for nuclear molecular imaging and gene therapy: from bedside to bench and back. Theranostics 2:392–402. https://doi.org/10.7150/thno.3722.
9. Penheiter AR, Russell SJ, Carlson SK. 2012. The sodium iodide symporter (NIS) as an imaging reporter for gene, viral, and cell-based therapies. Curr Gene Ther 12:33–47. https://doi.org/10.2174/156652312799789235.
10. Dohan O, Carrasco N. 2003. Advances in Na(+)/I(-) symporter (NIS) research in the thyroid and beyond. Mol Cell Endocrinol 213:59–70. https://doi.org/10.1016/j.mce.2003.10.059.
11. Haddad D, Chen NG, Zhang Q, Chen CH, Yu YA, Gonzalez L, Carpenter SG, Carson J, Au J, Mittra A, Gonen M, Zanzonico PB, Fong Y, Szalay AA. 2011. Insertion of the human sodium iodide symporter to facilitate deep tissue imaging does not alter oncolytic or replication capability of a novel vaccinia virus. J Transl Med 9:36. https://doi.org/10.1186/1479-5876-9-36.
12. Kang JH, Chung JK. 2008. Molecular-genetic imaging based on reporter gene expression. J Nucl Med 49(Suppl 2):164S–179S. https://doi.org/10.2967/jnumed.107.045955.
13. Sun C, Gardner CL, Watson AM, Ryman KD, Klimstra WB. 2014. Stable, high-level expression of reporter proteins from improved alphavirus expression vectors to track replication and dissemination during encephalitic and arthritogenic disease. J Virol 88:2035–2046. https://doi.org/10.1128/JVI.02990-13.
14. Assiri A, McGeer A, Perl TM, Price CS, Al Rabeeah AA, Cummings DA, Alabdullatif ZN, Assad M, Almulhim A, Makhdoom H, Madani H, Alhakeem R, Al-Tawfiq JA, Cotten M, Watson SJ, Kellam P, Zumla AI, Memish ZA. 2013. Hospital outbreak of Middle East respiratory syndrome coronavirus. N Engl J Med 369:407–416. https://doi.org/10.1056/NEJMoa1306742.
15. Guery B, Poissy J, el Mansouf L, Sejourne C, Ettahar N, Lemaire X, Vuotto F, Goffard A, Behillil S, Enouf V, Caro V, Mailles A, Che D, Manuguerra JC, Mathieu D, Fontanet A, van der Werf S. 2013. Clinical features and viral diagnosis of two cases of infection with Middle East Respiratory Syndrome coronavirus: a report of nosocomial transmission. Lancet 381:2265–2272. https://doi.org/10.1016/S0140-6736(13)60982-4.
16. Bhatia PK, Sethi P, Gupta N, Biyani G. 2016. Middle East respiratory syndrome: a new global threat. Indian J Anaesth 60:85–88. https://doi.org/10.4103/0019-5049.176286.
17. de Wit E, Rasmussen AL, Falzarano D, Bushmaker T, Feldmann F, Brining DL, Fischer ER, Martellaro C, Okumura A, Chang J, Scott D, Benecke AG, Katze MG, Feldmann H, Munster VJ. 2013. Middle East respiratory syndrome coronavirus (MERS-CoV) causes transient lower respiratory tract infection in rhesus macaques. Proc Natl Acad Sci U S A 110:16598–16603. https://doi.org/10.1073/pnas.1310744110.
18. Yao Y, Bao L, Deng W, Xu L, Li F, Lv Q, Yu P, Chen T, Xu Y, Zhu H, Yuan

J, Gu S, Wei Q, Chen H, Yuen KY, Qin C. 2014. An animal model of MERS produced by infection of rhesus macaques with MERS coronavirus. J Infect Dis 209:236–242. https://doi.org/10.1093/infdis/jit590.

19. Johnson RF, Via LE, Kumar MR, Cornish JP, Yellayi S, Huzella L, Postnikova E, Oberlander N, Bartos C, Ork BL, Mazur S, Allan C, Holbrook MR, Solomon J, Johnson JC, Pickel J, Hensley LE, Jahrling PB. 2015. Intratracheal exposure of common marmosets to MERS-CoV Jordan-n3/2012 or MERS-CoV EMC/2012 isolates does not result in lethal disease. Virology 485:422–430. https://doi.org/10.1016/j.virol.2015.07.013.
20. Haagmans BL, van den Brand JM, Provacia LB, Raj VS, Stittelaar KJ, Getu S, de Waal L, Bestebroer TM, van Amerongen G, Verjans GM, Fouchier RA, Smits SL, Kuiken T, Osterhaus AD. 2015. Asymptomatic Middle East respiratory syndrome coronavirus infection in rabbits. J Virol 89: 6131–6135. https://doi.org/10.1128/JVI.00661-15.
21. Houser KV, Gretebeck L, Ying T, Wang Y, Vogel L, Lamirande EW, Bock KW, Moore IN, Dimitrov DS, Subbarao K. 2016. Prophylaxis with a Middle East respiratory syndrome coronavirus (MERS-CoV)-specific human monoclonal antibody protects rabbits from MERS-CoV infection. J Infect Dis 213:1557–1561. https://doi.org/10.1093/infdis/jiw080.
22. Agrawal AS, Garron T, Tao X, Peng BH, Wakamiya M, Chan TS, Couch RB, Tseng CT. 2015. Generation of a transgenic mouse model of Middle East respiratory syndrome coronavirus infection and disease. J Virol 89: 3659–3670. https://doi.org/10.1128/JVI.03427-14.
23. Pascal KE, Coleman CM, Mujica AO, Kamat V, Badithe A, Fairhurst J, Hunt C, Strein J, Berrebi A, Sisk JM, Matthews KL, Babb R, Chen G, Lai KM, Huang TT, Olson W, Yancopoulos GD, Stahl N, Frieman MB, Kyratsous CA. 2015. Pre- and postexposure efficacy of fully human antibodies against Spike protein in a novel humanized mouse model of MERS-CoV infection. Proc Natl Acad Sci U S A 112:8738–8743. https://doi.org/10.1073/pnas.1510830112.
24. Zhao J, Li K, Wohlford-Lenane C, Agnihothram SS, Fett C, Zhao J, Gale MJ, Jr, Baric RS, Enjuanes L, Gallagher T, McCray PB, Jr, Perlman S. 2014. Rapid generation of a mouse model for Middle East respiratory syndrome. Proc Natl Acad Sci U S A 111:4970–4975. https://doi.org/10.1073/pnas.1323279111.
25. Cockrell AS, Yount BL, Scobey T, Jensen K, Douglas M, Beall A, Tang XC, Marasco WA, Heise MT, Baric RS. 2016. A mouse model for MERS coronavirus-induced acute respiratory distress syndrome. Nat Microbiol 2:16226. https://doi.org/10.1038/nmicrobiol.2016.226.
26. Khoshnevisan A, Jauregui-Osoro M, Shaw K, Torres JB, Young JD, Ramakrishnan NK, Jackson A, Smith GE, Gee AD, Blower PJ. 2016. [(18)F]tetrafluoroborate as a PET tracer for the sodium/iodide symporter: the importance of specific activity. EJNMMI Res 6:34. https://doi.org/10.1186/s13550-016-0188-5.
27. Niu G, Gaut AW, Ponto LL, Hichwa RD, Madsen MT, Graham MM, Domann FE. 2004. Multimodality noninvasive imaging of gene transfer using the human sodium iodide symporter. J Nucl Med 45:445–449.
28. Zuckier LS, Dohan O, Li Y, Chang CJ, Carrasco N, Dadachova E, Dohan O. 2004. Kinetics of perrhenate uptake and comparative biodistribution of perrhenate, pertechnetate, and iodide by NaI symporter-expressing tissues in vivo. J Nucl Med 45:500–507.
29. Menachery VD, Mitchell HD, Cockrell AS, Gralinski LE, Yount BL, Jr, Graham RL, McAnarney ET, Douglas MG, Scobey T, Beall A, Dinnon K, III, Kocher JF, Hale AE, Stratton KG, Waters KM, Baric RS. 2017. MERS-CoV accessory ORFs play key role for infection and pathogenesis. mBio 8:e00665-17. https://doi.org/10.1128/mBio.00665-17.
30. Scobey T, Yount BL, Sims AC, Donaldson EF, Agnihothram SS, Menachery VD, Graham RL, Swanstrom J, Bove PF, Kim JD, Grego S, Randell SH, Baric RS. 2013. Reverse genetics with a full-length infectious cDNA of the Middle East respiratory syndrome coronavirus. Proc Natl Acad Sci U S A 110:16157–16162. https://doi.org/10.1073/pnas.1311542110.
31. Johnson RF, Bagci U, Keith L, Tang X, Mollura DJ, Zeitlin L, Qin J, Huzella L, Bartos CJ, Bohorova N, Bohorov O, Goodman C, Kim DH, Paulty MH, Velasco J, Whaley KJ, Johnson JC, Pettitt J, Ork BL, Solomon J, Oberlander N, Zhu Q, Sun J, Holbrook MR, Olinger GG, Baric RS, Hensley LE, Jahrling PB, Marasco WA. 2016. 3B11-N, a monoclonal antibody against MERS-CoV, reduces lung pathology in rhesus monkeys following intratracheal inoculation of MERS-CoV Jordan-n3/2012. Virology 490:49–58. https://doi.org/10.1016/j.virol.2016.01.004.
32. Kumar M, Mazur S, Ork BL, Postnikova E, Hensley LE, Jahrling PB, Johnson R, Holbrook MR. 2015. Inactivation and safety testing of Middle East Respiratory Syndrome Coronavirus. J Virol Methods 223:13–18. https://doi.org/10.1016/j.jviromet.2015.07.002.
33. de Kok Mercado F, Kutlak F, Jahrling PB. 2011. The NIAID Integrated Research Facility at Fort Detrick. Appl Biosaf 16:58–66. https://doi.org/10.1177/153567601101600202.
34. National Research Council. 2011. Guide for the care and use of laboratory animals, 8th ed. National Academies Press, Washington, DC.